J Mater Sci: Mater Electron (2022) 33:23362–23374

Impact of copper doping in NiO thin films deposited by spray pyrolysis on their physical properties

A. Javadian[1] and M. R. Fadavieslam[1,*]

[1] School of Physics, Damghan University, Damghan, Iran

Received: 18 February 2022
Accepted: 7 September 2022
Published online:
29 September 2022

© The Author(s), under exclusive licence to Springer Science+Business Media, LLC, part of Springer Nature 2022

ABSTRACT

In this study, pure Cu-doped NiO thin films were deposited on glass substrates of soda lime by chemical spray pyrolysis. The effects of Cu-doping on the structural, optical, and electrical properties of the thin films were investigated by X-ray diffraction (XRD), field emission scanning electron microscopy with energy dispersive X-ray analyzer (FE-SEM–EDX), atomic force microscopy (AFM), ultraviolet–visible spectroscopy, and electrical resistance; van der Pauw techniques were also used to measure the Hall effect. Studies on X-ray diffraction showed that the films contained only one nickel oxide phase and were polycrystalline in a cubic crystal structure with preferred orientations along (111). Other orientations were along the (200) and (220) planes. In general, the FE-SEM and AFM images also showed that as Cu-doping increased, the grain size and surface roughness of the thin films decreased. The expected elemental compositions were confirmed by EDX. In the Raman spectra of the thin films, there were two peaks at 530 cm^{-1} and 1100 cm^{-1} that confirmed the presence of NiO on the films. The optical bandgap of the thin films decreased from 3.09 to 2.21 eV as Cu-dopant increased. As the Cu-doping concentration increased from 0 to 0.16 (at.%), the electrical resistance, carrier mobility, and activation energy decreased from 1.88×10^3 to 430 Ω.cm, 18.1 to 4.9 $cm^2/v.s$, and 0.245 to 0.203 eV, respectively; conversely, the carrier concentration increased from 1.84×10^{14} to 29.64×10^{14}. Hall effect studies showed that the films exhibited *p*-type conductivity.

1 Introduction

Optoelectronic devices are widely used in today's life, and it is impossible to imagine life without them. Transparent conductive oxides (TCOs) are widely used in the optoelectronic industry [1, 2]. When TCOs are used in optoelectronic devices, they must have high conductivity and good transmittance [3]. In the last few decades, developments in TCOs have been focusing on indium-tin oxide (ITO), fluorine-doped tin oxide (FTO), indium-doped zinc oxide (IZO), gallium-doped zinc oxide (GZO), and zinc oxide (ZnO), which are only n-type semiconductors due to oxygen vacancies and anion interstitials that generate

Address correspondence to E-mail: m.r.fadavieslam@du.ac.ir

https://doi.org/10.1007/s10854-022-09098-5

free electrons [4–6]. Nevertheless, researchers have always looked for p-type TCOs which have both a decent stability and also high conductivity [3]. Nickel oxide is a transparent conductive oxide material with p-type conductivity [7]. This is due to pure stoichiometric NiO is an insulator with a resistivity at room temperature on the order of 10^{13} Ω cm, when non-stoichiometric NiO exhibits p-type conductivity is with Ni^{3+} ions resulting from Ni^{2+} vacancies and/or interstitial oxygen in NiO crystallites [4, 8]. In other words,: Ni vacancies form easily and act as acceptors [9]. Among other properties, it has a wide bandgap of 3.6 to 4 eV, NaCl crystal structure, high chemical ductility and stability, excellent durability, and low material cost [10–15]. These properties give NiO good optical, electrical, thermoelectric, and catalytic properties [16, 17]. The physical properties of NiO thin films can be enhanced/improved by doping with elements such as Mn [18], In [19], Re, Pt [20], Li [21], B [22], La [23], Tb [24], Nd [10], Co [25], Zn [26], Na [27], Au [28], Ti [29], Cd [30], Sn [31], Al [32], Yb [33], Cr [34], Ag [35], Fe [36], Mg [37], Ce [38], N [39], Bi [2], Nb [40], and Y [41]. The results indicate that the surface morphology, crystal composition, uniformity, and physical properties of the thin films, like resistivity and transparency, depend on the nature and amount of the dopant [42]. For the application of nickel oxide thin films in optoelectronic devices, it is important to improve these properties. This can be achieved by doping with copper [28, 33, 35]. The copper can create different impurity levels that change the optical and electrical properties of the semiconductor [43]. In other words, copper creates microstructural defects, such as nickel vacancies and interstitial oxygen in NiO, which can affect the conductivity of the NiO thin film [4]. Copper is of more importance to researchers because of its special properties among these materials. The ionic radius and electronegativity of Ni^{2+} and Cu^{2+} are of the same order. This information suggests that Cu^{2+} ions can replace Ni^{2+} ions in the crystalline structure of NiO and further improve its electrical properties [4]. The decrease in resistivity could be attributed to the efficient substitution of Ni^{2+} by Cu^{2+} ions [4]. Doping of NiO thin films with Cu can be useful for a wide range of applications.

In this study, copper-doped NiO thin films were prepared by spray pyrolysis, and the structural, optical, and electrical properties of the films were investigated as a function of copper concentration. Most previous studies have investigated the effect of copper doped up to 8% [44, 45]. Therefore, we decided to investigate the effect of copper doping up to 16%. The physical properties of the films were investigated using XRD, FE-SEM, AFM, UV–vis spectroscopy, and the Hall system.

2 Experimental details

2.1 Film preparation

A precursor solution was prepared for each thin-film deposition by dissolving 2.3769 g of nickel chloride [$NiCl_2 6H_2O$] in 100 ml of deionized water. The molarity of nickel in the spray solution was 0.1 M. Copper chloride [$CuCl_2 2H_2O$] was dissolved in the forerunner solution. The atomic ratio of Copper per Nickel or $\frac{[Cu]}{[Ni]}$ (at.%) was changed from 0 to 4, 8, 12, and 16 at.% to study the effects of Cu add-up on the film due to physical properties. Each solution was stirred well and heated at room temperature for about 45 min until it became bright and sprayable. The solutions were applied to a soda-lime substrate under similar conditions: 30 cm distance between the nozzle and the substrate, 30 rpm rotation speed of the hot plate, 3 atm pressure of the carrier gas, 2.5 ml/min spray rate, 460 °C substrate temperatures, and accuracy of ± 2 °C controlled by a digital temperature controller. Preceding film fabrication, ethanol was used to clean the glass substrates. It was done in an ultrasonic bath for 15 min on a hot plate. The system was then allowed to cool to room temperature for about 80 min. A typical spray pyrolysis coating system was used to prepare the thin films [44].

2.2 Sample characterization

The crystal structures of the thin films were characterized using the XRD technique. The XRD instrument was a D8 Advance Bruker X-ray diffractometer with a Cu tube producing Cu-K_α radiation (k = 0.154056 nm) in a 2θ range of 10°-70°. The surface morphology of the samples was observed via FE-SEM using MIRA3 TESCAN. The cross-sectional FE-SEM image was also used to estimate the thickness of the thin films. The topology of the films was observed using an atomic force microscope (JPK-Nano Wizard II). Raman spectra were recorded between 250 and 3500 cm^{-1} using 532i Avantes Raman microscope.

The transmittance and reflectance spectra of the thin films were measured using the UV–Vis. (300–1100 nm) spectrophotometer, Shimadzo-1800. An Ecopia HMS-7000 Photonic Hall Effect Measurement System was used for electrical measurements.

3 Results and discussion

3.1 Structural characterization

Figure 1 shows the XRD patterns of the undoped and copper-doped NiO thin films. As can be seen, the numerous diffraction peaks in the diffraction patterns indicate a polycrystalline nature with broad humps, a cubic phase, and a preferential orientation along the (111) direction of the pure NiO phase [43, 45, 46]. Other peaks corresponding to other phases of Ni and Cu or/and CuO could not be detected, which means that no secondary phases were formed, and the copper atoms were successfully incorporated into the nickel sites of the NiO lattice. This could be because the ionic radii of Cu (0.73 Å) and Ni (0.69 Å) are comparable, and, therefore, copper ions can be easily replaced by nickel ions without causing significant lattice distortions [5, 46, 47]. Moreover, the preferred alignment does not change with copper doping [44]. In general, the intensity of the peaks decreased with copper doping, which could be due to an increase in point defects resulting from copper impurities [47, 48]. Figure 1 shows that the in-plane position of

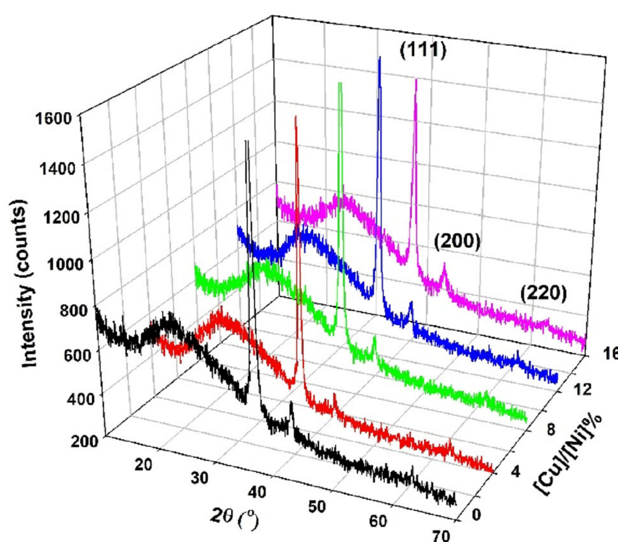

Fig. 1 XRD patterns for the NiO:Cu thin films at different Cu concentration

the XRD peak (111) shifts to a higher 2θ value at 4 and 8 at% copper doping, but at 12 and 16 at% copper doping, the peak position shifts to a lower 2θ value. This is likely due to the fact that at lower amounts of copper doping, Cu^{3+} (ionic radii equal to 0.54 Å) replaces Ni^{3+} (ionic radii equal to 0.56 Å), and at higher amounts of copper doping, Cu^{2+} (ionic radii equal to 0.73 Å) replaces Ni^{2+} (ionic radii equal to 0.69 Å). Some weak reflection peaks such as (200) and (220) were also observed, which could be attributed to poor crystallization [49]. The in-plane XRD peak (220) is weak or has not been observed in most previous studies [46, 50].

The peaks (111), (200), and (220) are located at 37.29°, 43.67°, and 63.73°, respectively, for thin films. The diffraction peaks obtained agree well with the JCPDS Card Number 14–0481 [12]. It is clear that all samples show the same structural pattern only the intensity varies. This could be a good indicator for the crystallinity of the film [12].

The interplanar spacings of the given Miller indices h, k, and l, d_{hkl} values of the NiO thin films were also calculated using the Bragg equation:

$$2d_{hkl}\sin\theta = n\lambda \tag{1}$$

where n is the diffraction order (usually n = 1) and λ is the X-ray wavelength. The lattice constant (a) was calculated using the following equation [51]:

$$\frac{1}{d_{hkl}^2} = \frac{h^2 + k^2 + l^2}{a^2} \tag{2}$$

Lattice parameter a for the cubic phase was calculated via (111) orientations. The average crystal grain size (D) was estimated using [52]:

$$D = \frac{0.94}{\beta\cos\theta} \tag{3}$$

where β is the width of the x-ray peak on the 2θ axis, normally measured as full width at half maximum (FWHM) after the error due to instrumental broadening has been properly corrected (subtraction of variances), θ is the Bragg angle. the dislocation density (δ) and strain (ε) were calculated using the following relations [13]:

$$\delta = \frac{1}{D^2} \tag{4}$$

$$\varepsilon = \frac{\beta\cos\theta}{4} \tag{5}$$

where θ is the usual Bragg angle, and β is the full width at half maxima of the diffraction peaks. Table 1 shows and summarizes the structural parameters for (111) the crystallographic orientation of the deposited NiO thin films. The observed '*d*' and '*a*' values agree well with the standard 'd' and 'a' values. It can be seen from Table 1 that the interplanar spacing and the lattice parameter increase, and the average crystal grain size decreases as the copper concentration increases. Since the atomic radius of the copper ion is larger than that of the nickel ion, the lattice parameter increases with the substitution of Cu in place of Ni in the cubic NiO structure [5, 43, 53]. The decreased crystallite size due to the increase in copper doping can probably be explained by the Zener pinning effect, i.e., Cu atoms could act as obstacles and hinder the movement of grain boundaries, resulting in a decrease in grain growth [43].

FE-SEM is a suitable method to study the shape, size, and mechanism of particle grain growth. Figure 2 shows the surface morphology and cross section of the NiO:Cu thin films prepared with different copper concentrations. The FE-SEM morphologies of the thin films are alike and they exhibit spherical grains on their whole surface. The surface morphology of the deposited thin film appears quasi-smooth, with excellent adhesion, uniform surface with densely packed spherical grains, and utterly devoid of pinholes and major cracks on the film surface. A similar morphology can be seen for the NiO thin films reported in [42, 43, 50]. Moreover, the surface of the thin films is covered with inhomogeneous, randomly oriented, and clustered particles. However, the morphology of the thin films depends on the Cu concentration. The average grain size is estimated to be in the range of 30 nm. In generally, the grain size increases and then decreases as the Cu concentration increases. As shown in Fig. 2, a smooth film with a surface morphology is a basic requirement for applications in electronics, optoelectronics, and electrochromics [12, 54]. The thickness of the thin films was assessed from the cross-sectional FE-SEM micrographs, as you can see in Table 2. The elemental composition of the NiO:Cu thin films was decided by energy dispersive X-ray spectrometry (EDX), and the values are listed in Table 2. The fact that nickel and oxygen elements are in the samples is attributed to the effective formation of NiO. As expected in Table 2, the atomic percentage value of copper in the doped sample approves the incorporation of Cu^{2+} ions into the NiO lattice network. The EDX spectrum for 8% Cu-doped NiO thin films is shown in Fig. 3. By considering these results, it can be concluded that the Cu was successfully doped by the spray pyrolysis technique.

Figure 4 shows two- and three-dimensional microscopic images of the thin films deposited with different Cu concentrations. The surface characterization results of the films are summarized in Table 1. The AFM images and the results of the average roughness values of the thin films helped us to analyze the physical properties of the thin films. For example, they provided information about the interaction of the droplets with the substrate glass. These results show that the morphology of the thin films was a function of the Cu concentration. Table 1 shows that as the Cu concentration increases, the average roughness values of the thin films decrease [55]. This behavior is different for [Cu]/[Ni] = 16%. The change in roughness values due to copper doping is attributed to the fact that the incorporation of Cu leads to the agglomeration of crystallites in the pure NiO matrix and formation of clusters [56].

Table 1 Results of structural characterization of the thin films

$\frac{[Cu]}{[Ni]}$ %at	2θ (°)	FWHM (°)	Observed '*d*' values (nm)	Observed '*a*' values (nm)	D (nm)	$\delta \times 10^{15}$ (lines/m^2)	$\varepsilon \times 10^{-3}$ (lines^2 m^4)	average roughness (nm)
0	37.261	0.727	2.41124	4.17626	12	6.89	3.01	33.03
4	37.285	0.545	2.41266	4.17885	16	3.87	2.25	29.15
8	37.285	0.661	2.41302	4.17957	13	5.7	2.73	17.89
12	37.187	0.694	2.4182	4.18845	13	6.28	2.87	17.49
16	37.132	0.744	2.42189	4.19484	12	7.23	3.08	43.14

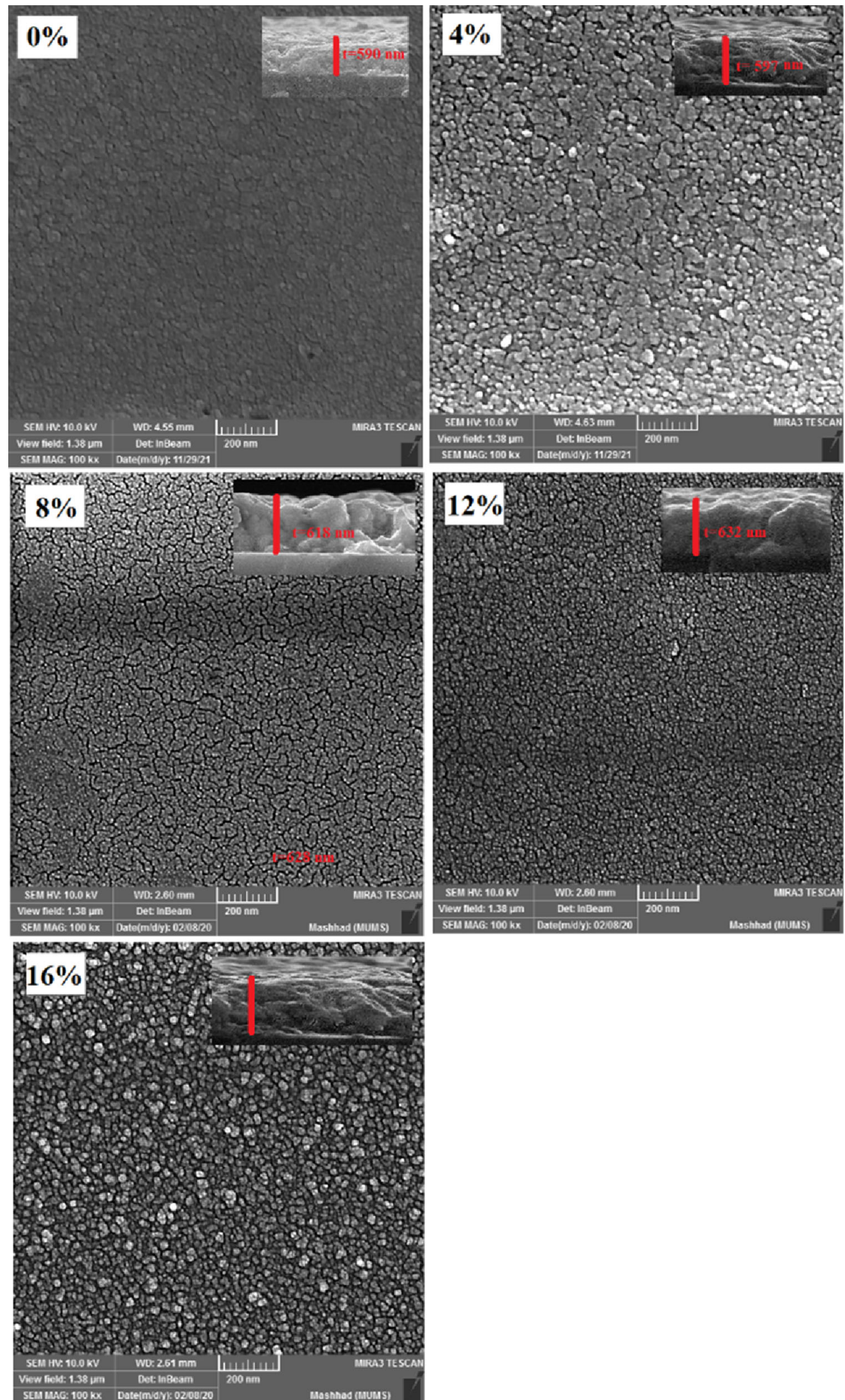

Fig. 2 Top view and cross section FE-SEM images for the NiO:Cu thin films at different Cu concentration

Table 2 Elemental compositions of the undoped and Cu-doped NiO films (including at% ratio)

$\frac{[Cu]}{[Ni]}\%(at)$ (at spray solution)	Result of EDX		
	O% (at)	Ni% (at)	Cu% (at)
4	71.65	27.17	1.18
8	62.68	34.68	2.64
12	61.89	34.19	3.92
16	61.46	33.42	5.12

3.2 Raman study

Figure 5 shows the Raman spectra of NiO and Cu-doped NiO at room temperature in the frequency range from 250 to 3500 cm^{-1}. Two prominent peaks around $\sim$ 530 cm^{-1} and $\sim$ 1100 cm^{-1} can be seen in the spectra of all thin films. A strong vibrational band of NiO associated with a phonon (1P) was observed at 530 cm^{-1} which clearly indicates the presence of the NiO transverse optical (TO) mode [57–59]. In addition, there are 2LO modes at 1100 cm^{-1} due to the vibrations of Ni–O bonds [30, 59]. This is due to the Ni–O stretching mode [12, 58]. The increase in the intensity of the (1P) LO peak in NiO is due to parity-breaking defects such as nickel vacancies and the crystallinity of the samples [59, 60]. It is evident that the intensity of the Raman peaks varies with doping with Cu relative to the XRD patterns. The increase in Raman shifts could be due to the increase in crystallite size of the Cu-doped NiO thin films [30].

3.3 Optical study

As a result of their unique optical properties, thin nickel oxide films are appropriate for a variety of optoelectronic applications. Many of these applications need high transparency in the UV–vis region. This can be attained by optimizing the parameters of the deposition layer, which are vital in the optical properties of NiO thin films. These properties are related to the oxygen vacancy, surface roughness, structure, crystalline quality, grain size, and thickness of the deposited thin films [12, 26, 34, 61–64]. Figure 6 shows the optical transmission spectra of NiO:Cu thin films deposited with different Cu concentrations. All films were examined in the wavelength range of 300–1100 nm at room temperature. It can be seen that the thin films have average transparency in the visible region of 22%, 24%, 31%, 34%, and 17% for undoped film, and 4%, 8%, 12%, and 16% doped films, respectively. It was observed that all the deposited samples have good transparency in the

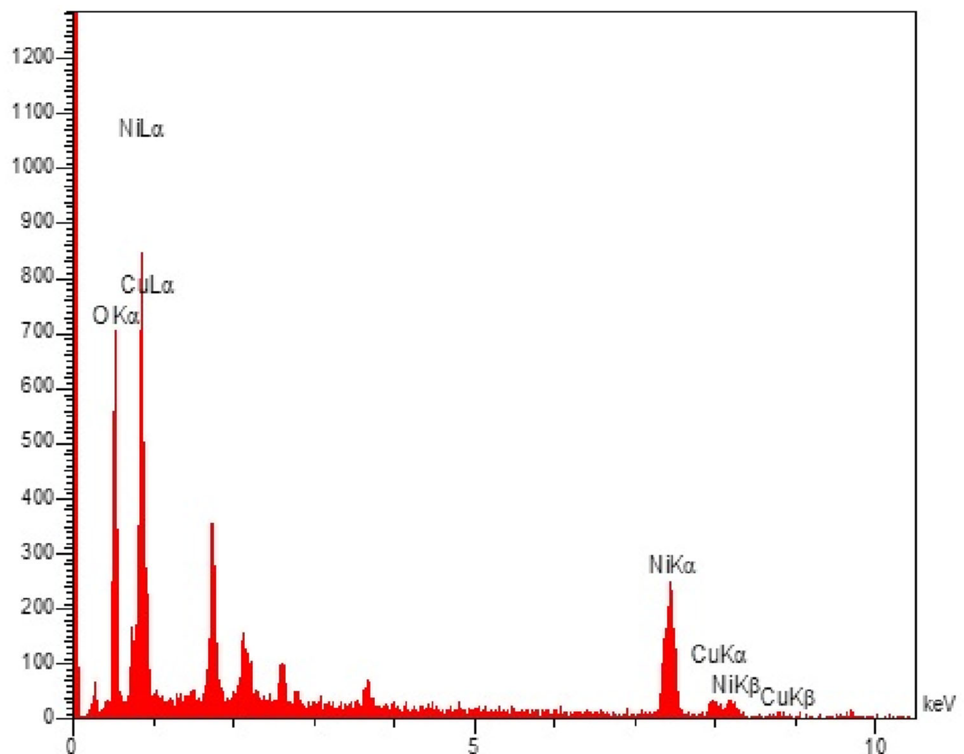

Fig. 3 EDX analysis of the NiO:Cu thin films prepared at 8% Cu-doped

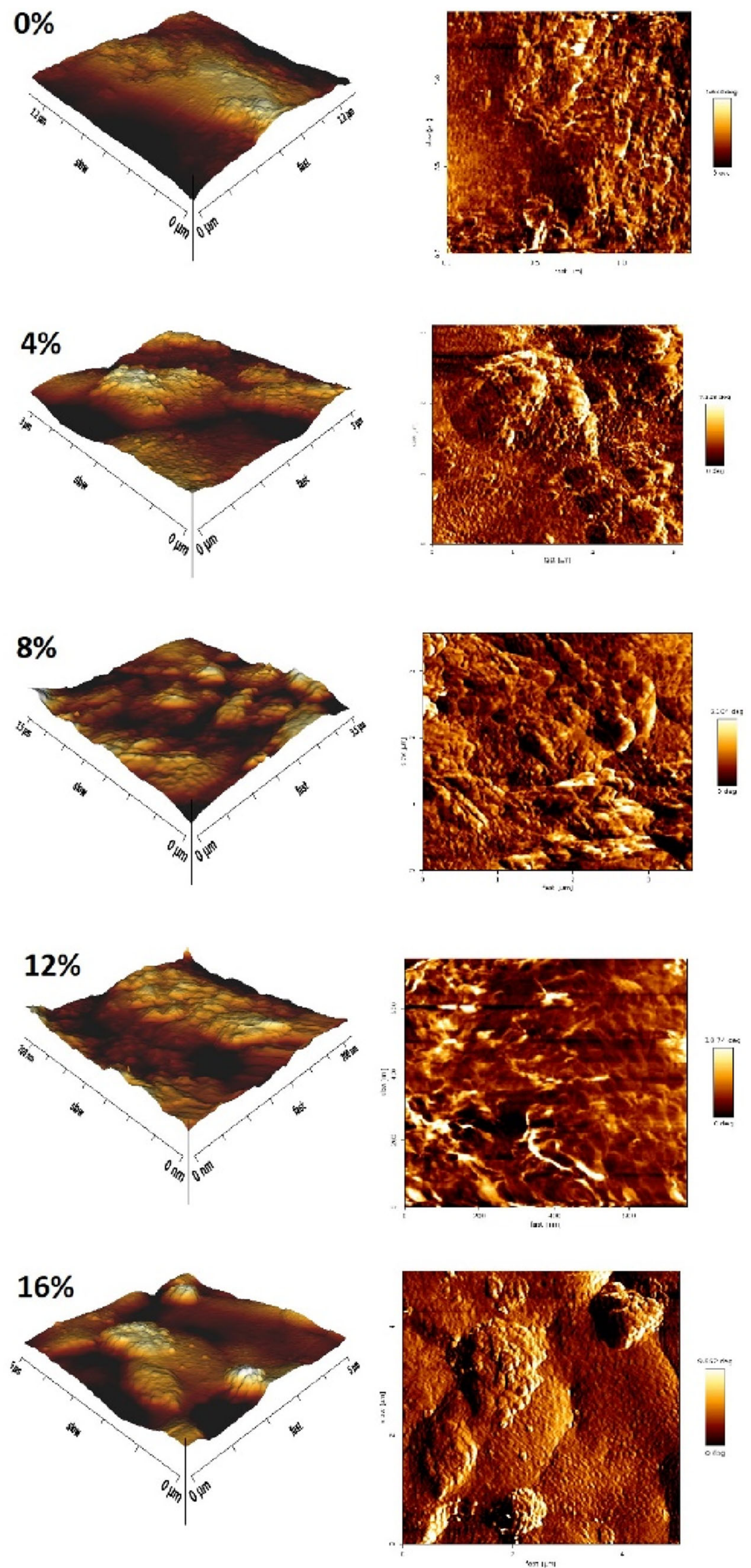

Fig. 4 AFM images for the NiO:Cu thin films at different Cu concentration

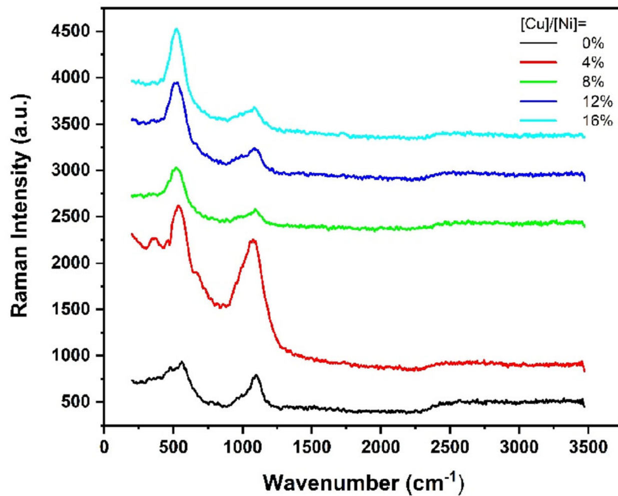

Fig. 5 Raman spectra at room temperature for the NiO:Cu thin films at different Cu concentrations

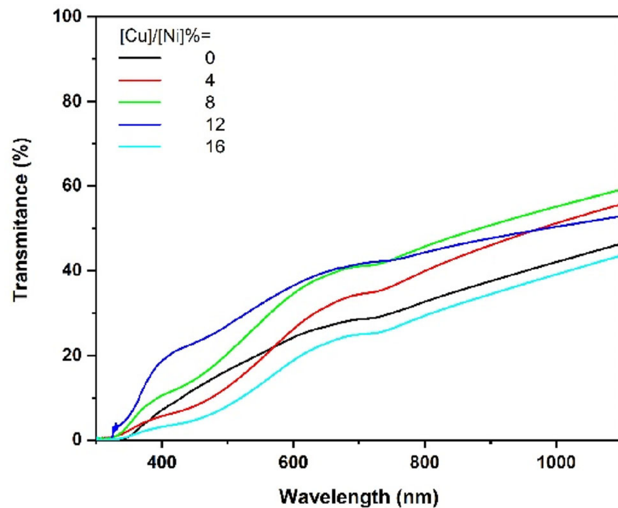

Fig. 6 The variation of transmittance as a function of wavelength for the NiO:Cu thin films at different Cu concentration

visible and near-infrared regions. All samples show ultimate absorption at wavelengths below ~ 380 nm because of the shift of electrons from the valence band to the conduction band [12, 21, 27, 65, 66]. Examination of Fig. 6 shows that the optical transmittance of the thin films increases as the Cu concentration increases [4]. The increasing optical transmittance is attributed to the increase in grain size with the increase in copper concentration [10, 61]. Accordingly, the decreasing surface roughness and increasing crystal grain size of the films show less scattering of incident light, resulting in increased transmittance [26, 67, 68].

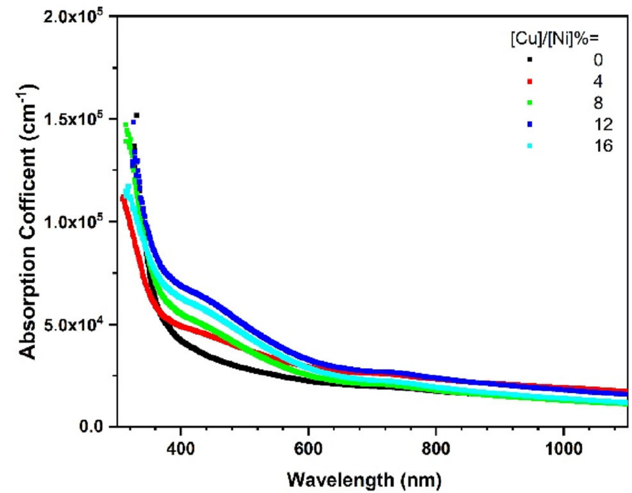

Fig. 7 Absorption coefficient spectra for the NiO:Cu thin films at different Cu concentration

The optical absorption coefficients are calculated using the following formula [69]:

$$\alpha = \frac{1}{d}\ln\left(\frac{(1-R)^2}{T}\right) \quad (6)$$

where α, d, R, and T are the thin films' absorbance coefficient, thickness, reflectance, and transmittance, respectively. Figure 7 shows the absorbance coefficient spectra of the NiO thin films deposited at different Cu concentrations. Examination of this figure shows that the Cu concentration affects the absorbance coefficient. The thin films have a low absorbance coefficient in the visible region and a strong absorbance coefficient in the lower wavelength region. Moreover, an absorption edge near (~380 nm) is observed in the thin films. The onset of the remarkable absorption is in the wavelength region below 380 nm, which provides excellent transparency for thin films in the visible region. In general, the absorbance coefficient changes as a function of crystalline properties, bandgap, surface roughness, and defect density [23, 26]. The direct optical bandgap can be obtained by optical absorption measurements by plotting $(\alpha h\vartheta)^2$ against the photon energy $h\vartheta$ and by means of the Tauc equation [41]:

$$(\alpha h\vartheta)^2 = \beta(h\vartheta - E_g) \quad (7)$$

where α, β, and E_g define the absorption coefficient, constant, and direct bandgap, respectively, as shown in Fig. 8, for the thin films prepared with Cu concentration. The bandgap values are estimated to be in the range of 2.21 to 3.09 eV. The obtained bandgap

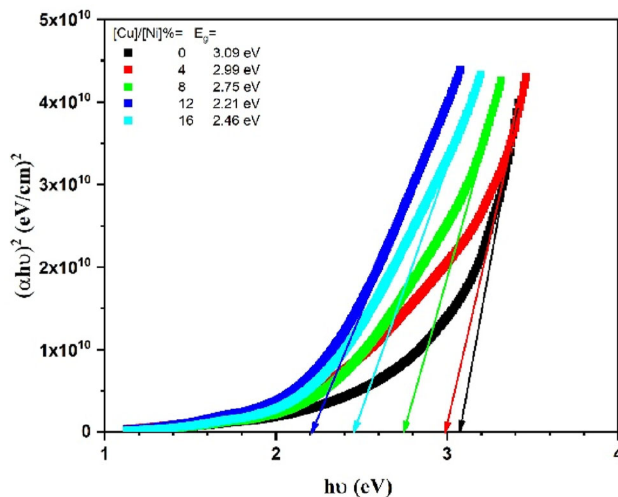

Fig. 8 Plots of $(\alpha h\vartheta)^2$ versus $h\vartheta$ for the NiO:Cu thin films at different Cu concentration

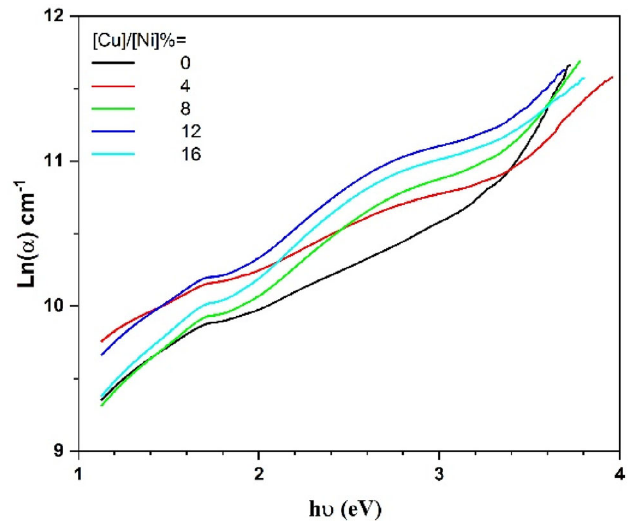

Fig. 9 Plots of ln(α) vs. $h\vartheta$ for the NiO:Cu thin films at different Cu concentration

values agree well with the previously published data [45, 70]. The optical bandgap values decreased with increasing Cu-doping and increased with Cu-doping up to 12% [17, 39, 46]. This behavior was reported by R. Balakarthikeyan et al. [43]. Increasing the film thickness leads to a decrease in the bandgap of the thin films [43, 50, 70]. This may also be due to CuO's much smaller bandgap vis-a-vis NiO [4]. In other words, the p-type Cu-dopant causes the narrowing of the bandgap in NiO because it can introduce holes into the valence band (VB) of NiO, which causes an upward shift in VB and a downward shift in the conduction band (CB) vis-a-vis pure NiO [43, 46].

We can study the disorder of the thin films by the changes in absorption coefficients [69]. The disparity of the absorption coefficient with photon energy is given by the empirical Urbach law [58]:

$$\alpha = \alpha_o \exp\left(\frac{h\vartheta}{E_U}\right) \quad (8)$$

where α_o is a constant, $h\vartheta$ is the photon energy, and E_U is the Urbach energy. The Urbach energy is an important parameter for characterizing the disorder and the width of the localized energy states in the material's bandgap [63, 66, 71, 72]. The Urbach tail emerges in poorly crystalline, disordered, and amorphous materials because of the localized states in these materials that widen or narrow the bandgap [72]. Moreover, the interaction between charge carriers and phonons is responsible for the Urbach band tail in semiconductor materials [58]. The Urbach energy of the NiO thin films was estimated from the slopes of Ln(α) versus photon energy $h\vartheta$ plots. The inverted slope of Ln(α) versus photon energy $h\vartheta$ plots determine the values of the Urbach energy. Figure 9 shows Ln(α) versus photon energy $h\vartheta$ plots of the thin films prepared with a Cu concentration. We used these figures, determined the thin films' Urbach energy, and summarized them in Table 3. Figure 10 shows the variation of the bandgap energy, Urbach energy, and activation energy as a function of Cu concentration. It is generally observed that the bandgap energy is inversely related to the Urbach energy [17, 21, 63].

3.4 Electrical properties

The electrical properties of the thin films were measured by using a Hall effect system under van der Pauw then they were summarized in Table 3. The Hall effect confirmed that all films were p-type [50, 73]. The compositional change, especially the formation of Ni^{2+}vacancies, leads to p-type conductivity of the thin films [57, 74, 75]. The resistivity of the NiO:Cu thin films decreased as the Cu concentration increased [17, 45, 50, 73]. In contrast, the concentration of holes increased when the Cu concentration increased. This is probably due to the efficient substitution of Cu^{+} in Ni^{2+} sites, which induces Ni^{2+}-Ni^{3+} intervalence charge transfer transitions and increases the hole concentration, decreasing the electrical resistivity of the thin films [17, 50, 73]. The study Table 3 shows that the carrier mobility decreases with increased Cu concentration. This can be ascribed to the higher density of the scattering centers of ionized impurities in the thin films [17].

Table 3 Results of optical and electrical characterization of thin films

$\frac{[Cu]}{[Ni]}\%at$	t (nm)	Eg (eV)	Urbach energy (eV)	Activation energy (eV)	Sheet Resistance ($\times 10^7$ Ω/sq)	ρ ($\times 10^3$ Ω.cm)	p ($\times 10^{14}$ cm^{-3})	μ (cm^2/v.s)
0	590	3.09	0.47	0.245	3.18	1.88	1.84	18.104
4	597	2.99	0.93	0.236	1.88	1.12	5.9	9.46
8	618	2.75	0.6	0.227	1.31	0.81	16.97	3.11
12	632	2.21	0.84	0.211	0.93	0.59	24.78	4.27
16	628	2.46	1.04	0.203	0.68	0.43	29.64	4.9

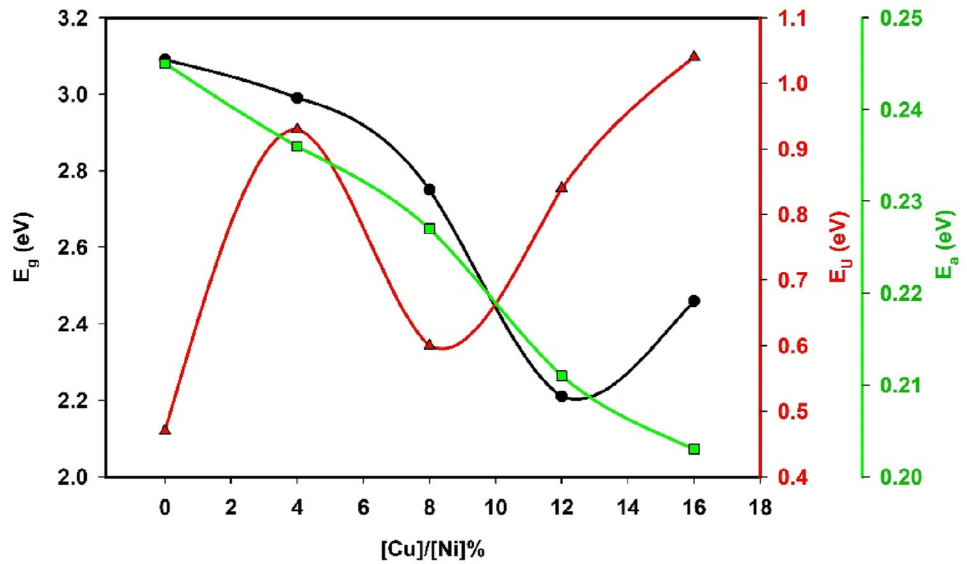

Fig. 10 Variations of the optical gap, Urbach energy, and activation energy as a function of Cu concentration

The temperature dependence of the electrical resistance of the thin films was measured in the temperature range 300–525 k in an air atmosphere to estimate the thermal activation energy. These data were fitted to the Arrhenius equation [76]:

$$R = R_o \exp^{\frac{E_a}{k_B T}}$$

where R_o is a parameter that depends on the properties of the sample (thickness, structure, etc.), E_a denotes the thermal activation energy of electrical resistance, and k_B is the Boltzmann constant. The plots $\mathrm{Ln}(R)$ versus $\frac{1000}{T}$ of the thin films are shown in Fig. 11. Table 3 summarizes the values of activation energy E_a gotten from the slope in the plots. It was found that the activation energy decreases as copper concentration increases from 0.245 to 0.203 eV. This indicates that the width of the energy bandgap decreases due to copper which lowers the resistivity and increases the conductivity of the copper-doped NiO thin films This is not contradicting with the increase in copper concentration This indicates that the

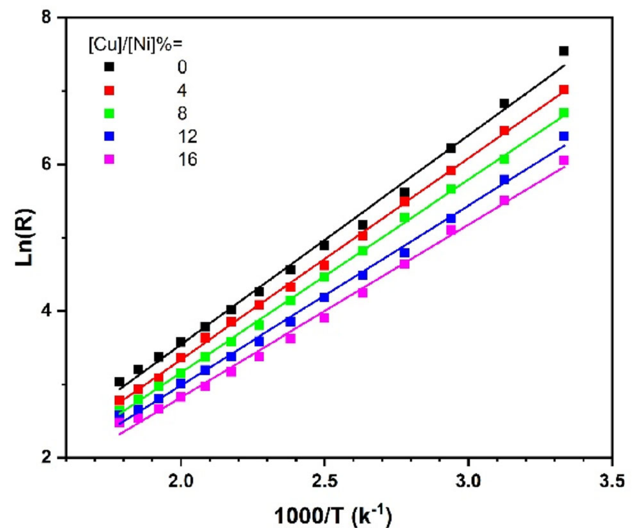

Fig. 11 Variation of resistance versus $\frac{1000}{T}$ for the NiO:Cu thin films at different Cu concentration

density of states at the Fermi level increases as copper concentrates more. The above results reveal the hopping of charge carriers between randomly distributed localized electronic states in the NiO samples [45]. Examination of these plots also shows that the resistance of the thin films decreases with an increase in temperature. This indicates that the films exhibit semiconductor-like behavior because an increasing number of dopants are ionized, and charge carriers are carried from the dopant levels to the band [73].

4 Conclusion

In this work, Pure NiO and NiO:Cu thin films were prepared by spray pyrolysis on a glass substrate. The effects of Cu-doping concentration on the thin films' structural, optical, and electrical properties were investigated. XRD characterization shows that all films have a cubic polycrystalline structure with a dominant orientation along the (111) direction. The crystallite size of the thin films decreased as Cu concentration increased. The FE-SEM morphologies of the thin films are similar and show spherical grains on their entire surface. The optical bandgap decreased as Cu concentration increased. The thin films were well suited with decent electrical properties and high transparency. The thin films exhibited p-type conduction. Therefore, they are suitable for applications such as TCO in thin-film solar cells.

Author contribution

All authors contributed to the study conception and design. Material preparation, data collection and analysis were performed by Abbas Javadian and Mohammad Reza Fadavieslam. The first draft of the manuscript was written by Mohammad Reza Fadavieslam and all authors commented on previous versions of the manuscript. All authors read and approved the final manuscript.

Funding

The authors declare that no funds, grants, or other support were received during the preparation of this manuscript.

Data availability

The datasets generated during and/or analyzed during the current study are available from the corresponding author on reasonable request.

Declarations

Conflict of interest The authors have no relevant financial or non-financial interests to disclose.

References

1. M.M. Gomaa, M. Boshta, B.S. Farag, M.B.S. Osman, J. Mater. Sci.: Mater. Electron. **27**, 711 (2016)
2. V. Ganesh, Opt. Laser Technol. **146**, 107579 (2022)
3. C.-K. Wen, Y.-Q. Xin, S.-C. Chen, T.-H. Chuang, P.-J. Chen, H. Sun, Thin Solid Films **677**, 103 (2019)
4. M. Das, A. Mukherjee, P. Mitra, J. Mater. Sci.: Mater. Electron. **29**, 1216 (2018)
5. I. Manouchehri, D. Mehrparvar, R. Moradian, K. Gholami, T. Osati, Optik **127**, 8124 (2016)
6. K. Sato, S. Kim, S. Komuro, X. Zhao, Jpn J. Appl. Phys. **55**, 06GJ10 (2016)
7. K. Nishimoto, K. Shima, S.F. Chichibu, M. Sugiyama, Jpn. J. Appl. Phys. **61**, 025505 (2022)
8. Y.A.K. Reddy, A.S. Reddy, P.S. Reddy, Phys. Scr. **87**, 015801 (2012)
9. Y.-J. Lin, T.-H. Su, P.-C. Kuo, H.-C. Chang, Mater. Chem. Phys. **276**, 125345 (2022)
10. V. Ganesh, B.R. Kumar, Y. Bitla, I.S. Yahia, S. AlFaify, J. Inorg. Organomet. Polym Mater. **31**, 2691 (2021)
11. A.A. Akl, S.A. Mahmoud, Optik **172**, 783 (2018)
12. S. Visweswaran, R. Venkatachalapathy, M. Haris, R. Murugesan, Appl. Phys. A **126**, 524 (2020)
13. R.S. Kate, S.C. Bulakhe, R.J. Deokate, J. Electron. Mater. **48**, 3220 (2019)
14. N. Srivastava, P. Srivastava, J. Mater. Sci.: Mater. Electron. **27**, 11478 (2016)
15. M. Terlemezoglu, O. Surucu, M. Isik, N.M. Gasanly, M. Parlak, Appl. Phys. A **128**, 50 (2021)
16. H.P. Parkhomenko, M.N. Solovan, A.I. Mostovoi, I.G. Orletskii, O.A. Parfenyuk, P.D. Maryanchuk, Opt. Spectrosc. **122**, 944 (2017)
17. M. Aftab, M.Z. Butt, D. Ali, F. Bashir, T.M. Khan, Opt. Mater. **119**, 111369 (2021)
18. N. Aswathy, J. Varghese, S.R. Nair, R.V. Kumar, Mater. Chem. Phys. **282**, 125916 (2022)

19. I. Raj, S. Valanarasu, A. Asuntha, R. Rimal Isaac, M. Shkir, H. Algarni, and S. AlFaify, Journal of Materials Science: Materials in Electronics, 1 (2022).
20. I. Garduno-Wilches, J. Alonso, Int. J. Hydrogen Energy **38**, 4213 (2013)
21. A. Kumar, P. Sahay, Appl. Phys. A **127**, 1 (2021)
22. U. Alver, H. Yaykaşlı, S. Kerli, A. Tanrıverdi, Int. J. Minerals Metallurgy, Mater. **20**, 1097 (2013)
23. C. Mrabet, M. Ben Amor, A. Boukhachem, M. Amlouk, T. Manoubi, Ceramics Internat. **42**, 5963 (2016)
24. M.D. Devi, A.V. Juliet, K. Hariprasad, V. Ganesh, H.E. Ali, H. Algarni, I. Yahia, Mater. Sci. Semicond. Process. **127**, 105673 (2021)
25. M. Ghougali, O. Belahssen, S. Benhamida, M. Mimouni, G. Rihia, M. Mahboub, and A. Beggas, Chalcogenide Letters **18** (2021).
26. R. Sharma, A.D. Acharya, S.B. Shrivastava, M.M. Patidar, M. Gangrade, T. Shripathi, V. Ganesan, Optik **127**, 4661 (2016)
27. Y. Aoun, M. Marrakchi, S. Benramache, B. Benhaoua, S. Lakel, and A. Cheraf, Materials Research **21** (2018).
28. H.K. Jung, S.J. Lee, D. Han, A.-R. Hong, H.S. Jang, S.H. Lee, J.H. Mun, H. Lee, S.H. Han, D. Yang, Electrochim. Acta **330**, 135203 (2020)
29. Y. Li, G.Y. Zhao, Z.B. Kou, J.C. Liu, R. Zhu, IOP Conference Series: Materials Science and Engineering **303**, 012007 (2018)
30. M.B. Amor, A. Boukhachem, A. Labidi, K. Boubaker, M. Amlouk, J. Alloy. Compd. **693**, 490 (2017)
31. T. Chtouki, L. Soumahoro, B. Kulyk, H. Erguig, B. Elidrissi, B. Sahraoui, Optik **136**, 237 (2017)
32. P. Baraskar, R. J. Choudhary, P. K. Sen, and P. Sen, in *Study of nonlinear optical absorption in undoped and Al doped NiO thin film*, 2020 (AIP Publishing LLC), p. 020161.
33. S. Zargouni, S. El Whibi, E. Tessarolo, M. Rigon, A. Martucci, H. Ezzaouia, Superlattices Microstruct. **138**, 106361 (2020)
34. M. Shkir, V. Ganesh, S. AlFaify, I. Yahia, H. Zahran, J. Mater. Sci.: Mater. Electron. **29**, 6446 (2018)
35. K.O. Egbo, C.E. Ekuma, C.P. Liu, K.M. Yu, Phys. Rev. Mater. **4**, 104603 (2020)
36. M. Shkir, M. Arif, V. Ganesh, A. Singh, H. Algarni, I. Yahia, S. AlFaify, Appl. Phys. A **126**, 1 (2020)
37. Y. Zhao, J. Yan, Y. Huang, J. Lian, J. Qiu, J. Bao, M. Cheng, H. Xu, H. Li, K. Chen, J. Mater. Sci.: Mater. Electron. **29**, 11498 (2018)
38. M. Arif, M. Shkir, V. Ganesh, A. Singh, H. Algarni, S. AlFaify, Superlattices Microstruct. **129**, 230 (2019)
39. V. Ganesh, L. Haritha, M. Anis, M. Shkir, I. Yahia, A. Singh, S. AlFaify, Solid State Sci. **86**, 98 (2018)
40. A. Farghali, W. Rouby, M. Abdel-Wahab, Digest J. Nanomater. Biostruct. **11**, 811 (2016)
41. I.L.P. Raj, S. Valanarasu, A.A. Abdeltawab, S.Z. Mohammady, M. Ubaidullah, S.F. Shaikh, M. Shkir, Optik **248**, 168105 (2021)
42. M. Najafi, H. Eshghi, Scientia Iranica **22**, 1317 (2015)
43. R. Balakarthikeyan, A. Santhanam, R. Anandhi, S. Vinoth, A.M. Al-Baradi, Z. Alrowaili, M. Al-Buriahi, K.D.A. Kumar, Opt. Mater. **120**, 111387 (2021)
44. M.R. Fadavieslam, J. Mater. Sci.: Mater. Electron. **28**, 2392 (2017)
45. S. Moghe, A. Acharya, R. Panda, S. Shrivastava, M. Gangrade, T. Shripathi, V. Ganesan, Renewable Energy **46**, 43 (2012)
46. Z.T. Khodair, B.A. Ibrahim, M.K. Hassan, Materials Today: Proceedings **20**, 560 (2020)
47. M. Aftab, M. Butt, D. Ali, F. Bashir, Z. Aftab, Ceram. Int. **46**, 5037 (2020)
48. R. Balakarthikeyan, A. Santhanam, R. Anandhi, S. Vinoth, A.M. Al-Baradi, Z.A. Alrowaili, M.S. Al-Buriahi, and K. Deva Arun Kumar, Optical Materials **120**, 111387 (2021)
49. R. Kate, S. Khalate, R. Deokate, J. Anal. Appl. Pyrol. **125**, 289 (2017)
50. S.M. Menaka, G. Umadevi, M. Manickam, Mater. Chem. Phys. **191**, 181 (2017)
51. A. Boukhachem, R. Boughalmi, M. Karyaoui, A. Mhamdi, R. Chtourou, K. Boubaker, M. Amlouk, Mater. Sci. Eng., B **188**, 72 (2014)
52. A. Alshahrie, I.S. Yahia, A. Alghamdi, P.Z. Al Hassan, Optik **127**, 5105 (2016)
53. S.-H. Wang, S.-R. Jian, G.-J. Chen, H.-Z. Cheng, J.-Y. Juang, Coatings **9**, 107 (2019)
54. F. Özütok, S. Demiri, and E. Özbek, in *Electrochromic NiO thin films prepared by spin coating*, 2017 (AIP Publishing LLC), p. 050011.
55. M. Aftab, M. Z. Butt, D. Ali, Z. H. Aftab, M. U. Tanveer, and B. Fayyaz, Environmental Science and Pollution Research, 1 (2021).
56. V. Ganesh, M. Shkir, M. Anis, S. AlFaify, Mater. Res. Express **6**, 086439 (2019)
57. C. Guillén and J. Herrero, physica status solidi (a) **218**, 2100237 (2021).
58. F. Chandoul, H. Moussa, K. Jouini, A. Boukhachem, F. Hosni, M.S. Fayache, R. Schneider, J. Mater. Sci.: Mater. Electron. **30**, 348 (2019)
59. S.T. Akinkuade, W.E. Meyer, J.M. Nel, Physica B **575**, 411694 (2019)
60. V.P.M. Shajudheen, V.S. Kumar, A.U. Maheswari, M. Sivakumar, S.S. Kumar, K.A. Rani, Materials Today: Proceedings **5**, 8577 (2018)

61. M.M. Gomaa, M.H. Sayed, V.L. Patil, M. Boshta, P.S. Patil, J. Alloy. Compd. **885**, 160908 (2021)
62. R. Sharma, A.D. Acharya, S.B. Shrivastava, T. Shripathi, V. Ganesan, Optik **125**, 6751 (2014)
63. A. Diha, S. Benramache, B. Benhaoua, Optik **172**, 832 (2018)
64. G. Atak, Ö.D. Coşkun, Solid State Ionics **305**, 43 (2017)
65. R. Barir, B. Benhaoua, S. Benhamida, A. Rahal, T. Sahraoui, R. Gheriani, J. Nanomater. **2017**, 1–10 (2017)
66. B. Maaoui, Y. Aoun, S. Benramache, A. Nid, R. Far, A. Touati, Adv. Mater. Sci. **20**, 79 (2020)
67. D.P. Joseph, M. Saravanan, B. Muthuraaman, P. Renugambal, S. Sambasivam, S.P. Raja, P. Maruthamuthu, C. Venkateswaran, Nanotechnology **19**, 485707 (2008)
68. H. Hakkoum, T. Tibermacine, N. Sengouga, O. Belahssen, M. Ghougali, A. Benhaya, A. Moumen, E. Comini, Opt. Mater. **108**, 110434 (2020)
69. Z.E. Khalidi, S. Fadili, B. Hartiti, A. Lfakir, P. Thevenin, M. Siadat, Opt. Quant. Electron. **48**, 427 (2016)
70. Y. Firat, A. Peksoz, Electrochim. Acta **295**, 645 (2019)
71. A. Loukil, A. Boukhachem, M. Ben Amor, M. Ghamnia, K. Raouadi, Ceram. Int. **42**, 8274 (2016)
72. M. Jamal, S. Shahahmadi, P. Chelvanathan, H.F. Alharbi, M.R. Karim, M.A. Dar, M. Luqman, N.H. Alharthi, Y.S. Al-Harthi, M. Aminuzzaman, Results in Physics **14**, 102360 (2019)
73. C.C. Singh, A.N. Roy Choudhury, D.S. Sutar, S.K. Sarkar, J. Appl. Phys. **129**, 095104 (2021)
74. S. Cheemadan, M.S. Kumar, Mater. Res. Express **5**, 046401 (2018)
75. S. Oh, Y.S. Park, P.J. Ko, N.-H. Kim, J. Nanosci. Nanotechnol. **18**, 6213 (2018)
76. M. Fadavieslam, N. Shahtahmasebi, M. Rezaee-Roknabadi, M. Bagheri-Mohagheghi, Phys. Scr. **84**, 035705 (2011)

Publisher's Note Springer Nature remains neutral with regard to jurisdictional claims in published maps and institutional affiliations.

Springer Nature or its licensor holds exclusive rights to this article under a publishing agreement with the author(s) or other rightsholder(s); author self-archiving of the accepted manuscript version of this article is solely governed by the terms of such publishing agreement and applicable law.